SITE CHARACTERIZATION REPORT
SGLK: Glarus (GL) - Kantonsspital

Manuel Hobiger, Donat Fäh

Last Modification: 26/02/2020

Schweizerischer Erdbebendienst (SED)
Service Sismologique Suisse
Servizio Sismico Svizzero
Servizi da Terratrembels Svizzer

ETH Zürich
Sonneggstrasse 5
8092 Zürich
Schweiz
manuel.hobiger@sed.ethz.ch

Contents

Summary

The free-field strong-motion station SGLK was built next to the Kantonsspital in Glarus. We performed a passive seismic array measurement to characterize the soil underneath the station.

The measurements show that the fundamental frequency of the structure beneath the station is about 1 Hz, but a second and stronger peak is found at around 2.4 Hz. The array measurements were analyzed with different techniques, namely 3-component HRFK, WaveDec and SPAC. The techniques gave different dispersion curves and our final interpretation is that WaveDec and SPAC retrieved the fundamental Love and Rayleigh wave dispersion curves, while HRFK found the curves for the first higher mode.

The joint inversion of the Love and Rayleigh wave dispersion curves for the fundamental and first harmonic modes and the Rayleigh wave ellipticity angle showed that the structure can be explained by models with interfaces at around 1 m, 9 m, 27 m and 60 m depth. The V_{S30} of the best models is about 394 m/s, corresponding to soil class B in EC8 and C in SIA261.

1 Introduction

In the framework of the second phase of the Swiss Strong Motion Network (SSMNet) renewal project, a new station was planned in the canton of Glarus.

The site selection resulted in the Kantonsspital as the best site. The new station, called SGLK, went operational on 19 July 2017. The location of the station is shown in Fig. 1.

Figure 1: Map showing the location of station SGLK in Glarus. ©2019 swisstopo (JD100042)

2   Geological setting

A geological map of the surroundings of station SGLK is shown in Fig. 2. According to the geological atlas, station SGLK and most stations of the passive array measurement lie on river gravels, while one station of the array lies on alluvial deposits.
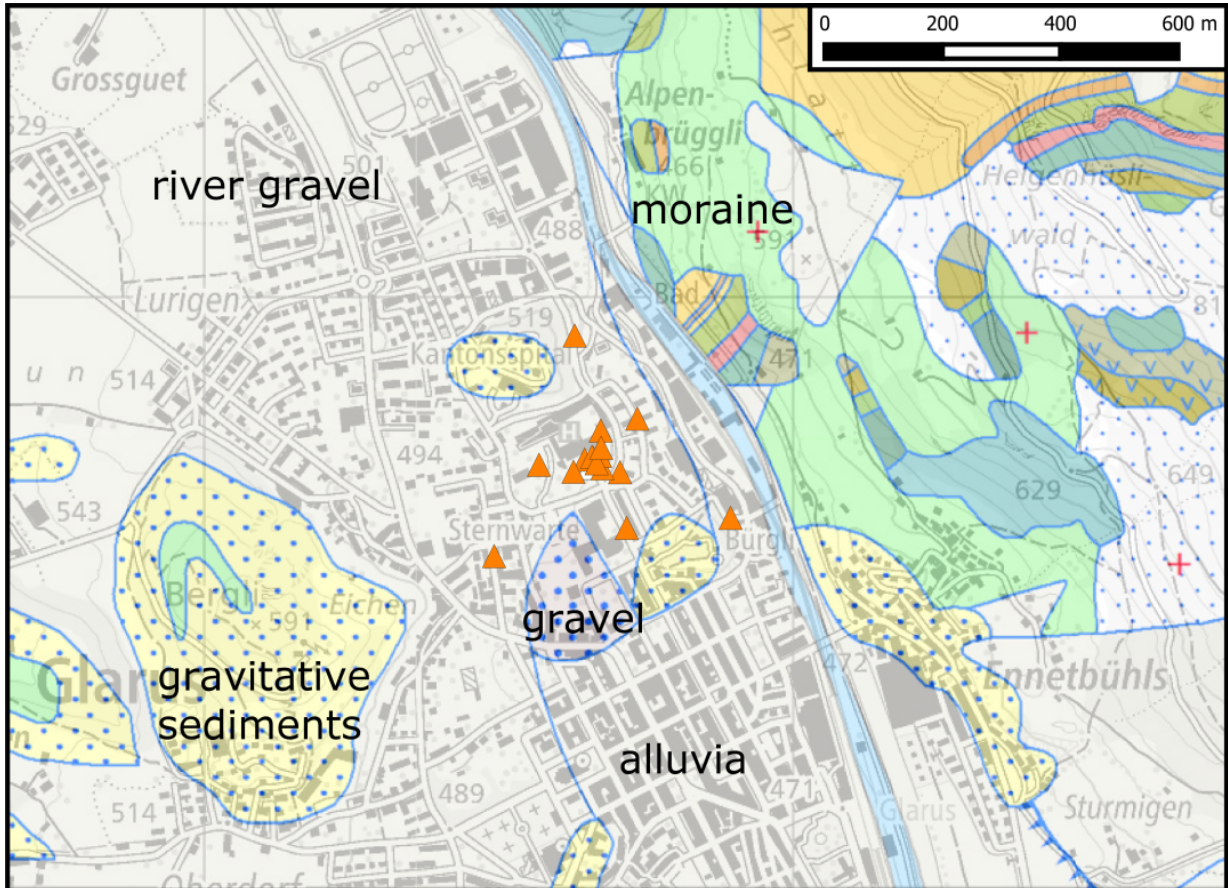

Figure 2: Geological map of the area around station SGLK. The stations of the passive seismic array are shown as orange triangles. ©2019 swisstopo (JD100042)

3 Site characterization measurements

3.1 Data set

In order to characterize the local underground structure around station SGLK, a passive seismic array measurement was carried out on 19 October 2017. The layout of the seismic measurements is shown in Fig. 3.

A single array measurement was performed. The array consisted of 16 stations. It was planned to consist of five rings of three stations each around a central station, which was located close to station SGLK. The ring radii were planned to be 8 m, 20 m, 45 m, 105 m, and 235 m, respectively. The final minimum and maximum inter-station distances in the array were 7.9 m and 406.9 m, respectively. The names of the stations of the array are composed of "SGLK" followed by a two-digit number (42 to 49, 52 to 55, 66, 67, 72, 74). The seismic stations consisted of Lennartz 3C 5 s sensors connected to Centaur digitizers. A total of 12 digitizers were used. Twelve sensors were connected to the A channels of the digitizers and another four sensors were connected to B channels. The total recording time was 160 minutes.

The station locations have been measured by a differential GPS system (Leica Viva GS10) which was set up to measure with a precision better than 5 cm. This precision was achieved for most stations. For two stations, the precision was worse: SGLK44 (12.0 cm), SGLK72 (16.9 cm).
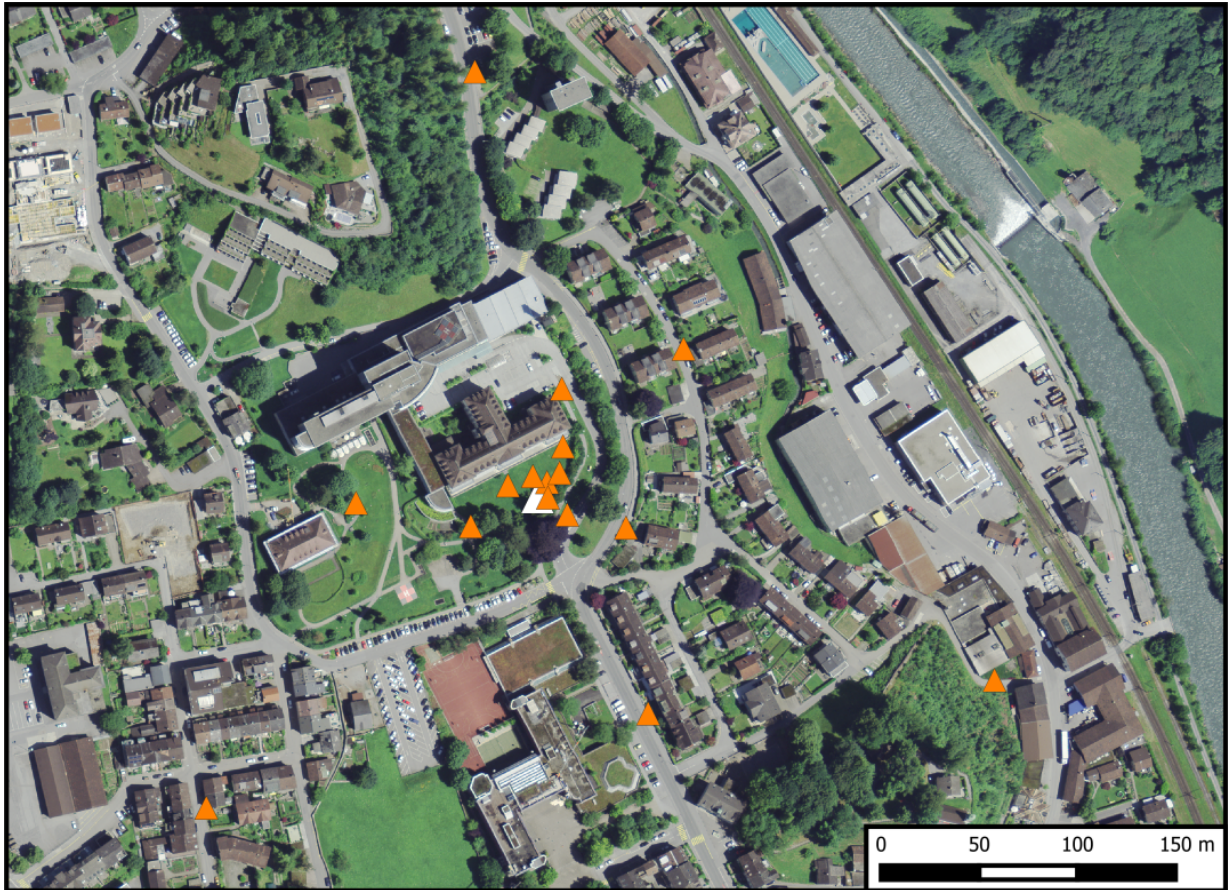
Figure 3: Layout of the array measurements around station SGLK. The location of SGLK is indicated by the white triangle, the locations of the stations for the passive seismic measurement by the orange triangles. ©2019 swisstopo (JD100042)

3.2 H/V and RayDec ellipticity curves

Figure 4 shows the H/V curves determined with the time-frequency analysis method (Fäh et al., 2009) for all stations of the passive array. All curves are very similar at low frequencies and only show major differences above 2 Hz. A first peak is picked between 1.05 and 1.17 Hz for most stations, with two outliers, where it is picked at 0.94 and 0.96 Hz, respectively. A second, more pronounced peak is picked between 2.29 and 2.49 Hz on the different stations. Above this peak, the different curves vary considerably. The RayDec technique (Hobiger et al., 2009) is supposed to eliminate the contributions of other wave types than Rayleigh waves and give a better estimate of the ellipticity than the classical H/V technique. The RayDec ellipticity curves for all stations of the array measurements are shown in Fig. 4. They are similar to the H/V curves. Station SGLK72, the station closest to station SGLK, serves as a reference and will be used for the inversion. This curve is the only one to show a very pronounced higher peak above 20 Hz.
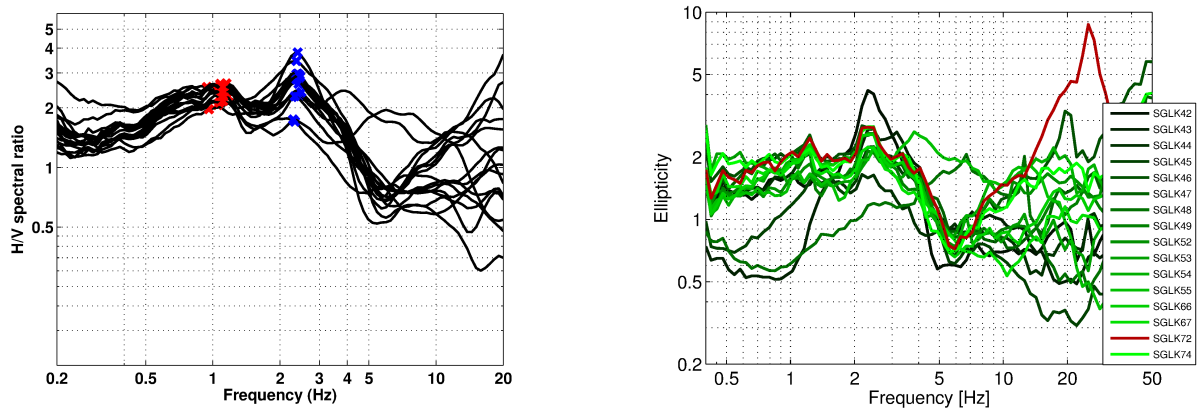

Figure 4: Left: Overview of the H/V measurements for the different stations of the array measurements. Right: RayDec ellipticities for all measurement stations. The red curve corresponds to SGLK72, the station closest to SGLK.

3.3 Polarization measurements

The polarization analysis was performed according to Burjánek et al. (2010) and Burjánek et al. (2012). The results for all stations of the array are similar. Only the results for SGLK72, the station in the array center, are shown here.

No preferential linear particle polarization is visible; we do not see indications for 2-dimensional polarization effects.
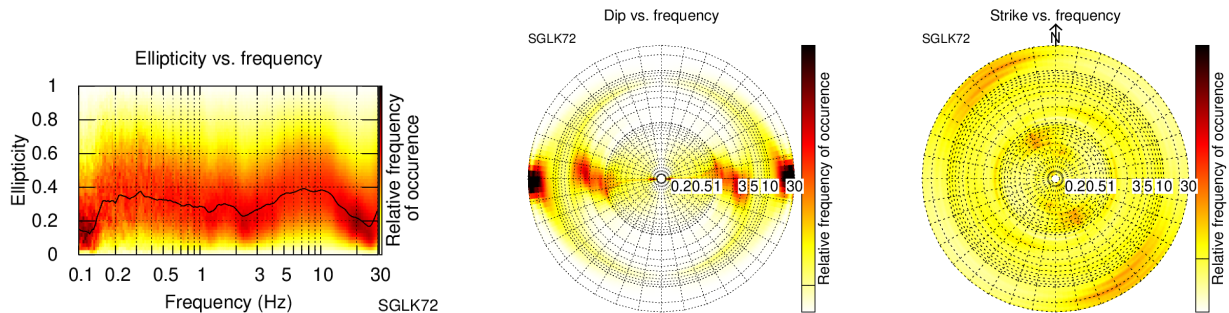

Figure 5: Polarization analysis of station SGLK44.

3.4 3-component high-resolution FK

The results of the 3-component high-resolution FK analysis (Poggi and Fäh, 2010) are shown in Fig. 6. On the transverse component, corresponding to Love waves, we can clearly identify a dispersion curve between 2.19 and 23.0 Hz. The upper-frequency resolution limit of the array is not reached, probably because no waves with sufficient energy are present at these frequencies.

On the vertical component, corresponding to Rayleigh waves, we can clearly identify one mode between 2.85 and 34.3 Hz, reaching the upper-frequency array resolution limit. On the radial component, also related with Rayleigh waves, we can identify one mode between 2.98 and 16.1 Hz.

The corresponding ellipticity curves of these modes are mostly flat over the entire frequency range.
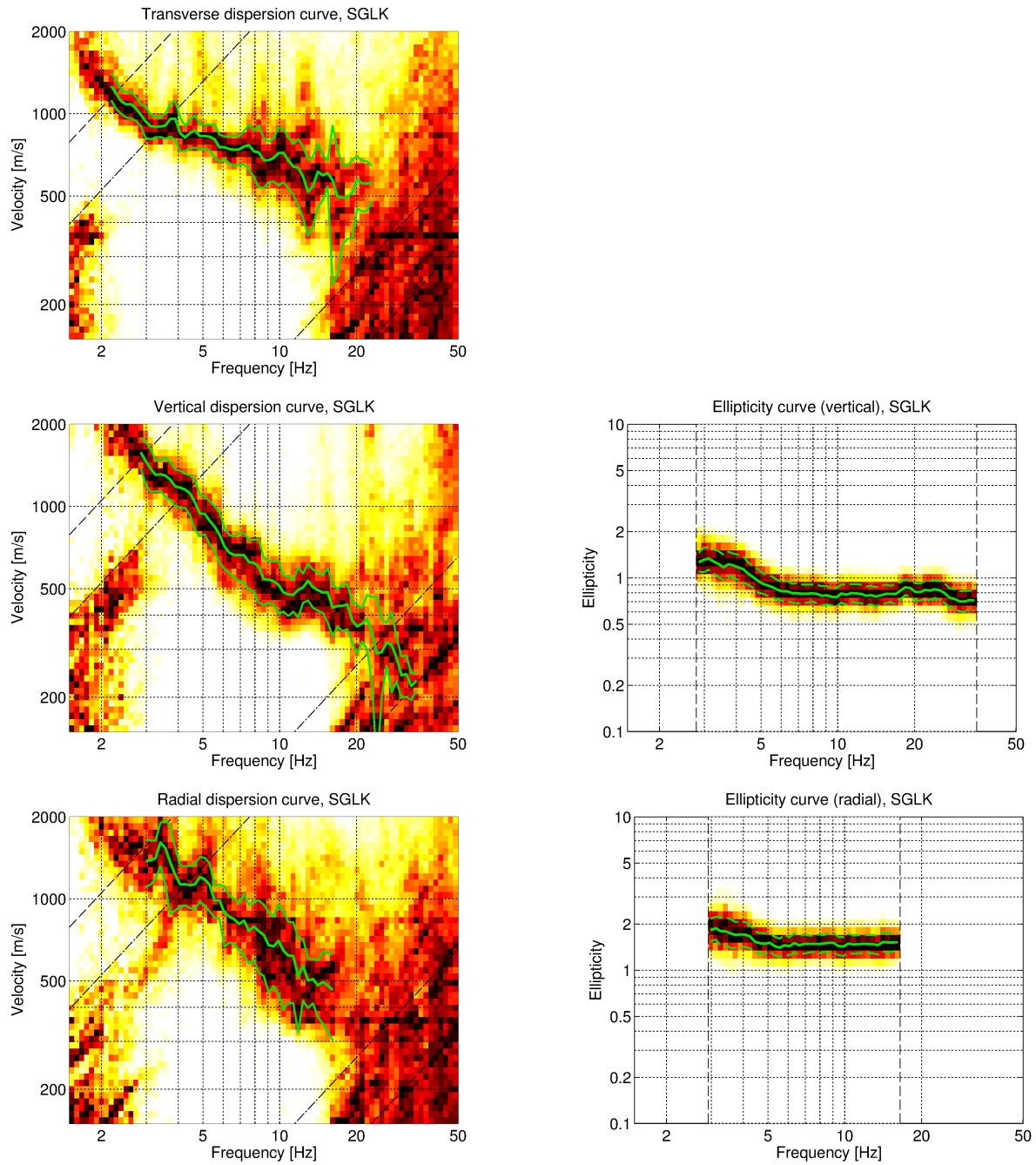
Figure 6: Dispersion and ellipticity curves obtained with the 3-component HRFK algorithm (Poggi and Fäh, 2010). In the left column, the dispersion curves for the transverse, vertical and radial components are shown, and in the right column the ellipticity curves corresponding to the dispersion curves picked on the vertical and radial components. The dashed and dotted black lines are the array resolution limits. The solid green lines are picked from the data, where the central line indicates the best values and the two outer lines the standard deviation.

11

3.5 WaveDec

The results of the WaveDec (Maranò et al., 2012) processing are shown in Fig. 7. This technique estimates the properties of single or multiple waves simultaneously with a maximum likelihood approach. In order to improve the results, the parameter γ, which modifies the sharpness of the wave property estimation, has been tuned. Here, a value of $\gamma = 0.2$ was used, corresponding to a predominantly maximum likelihood estimation. The Love wave dispersion curve is identified between 2.15 and 16.9 Hz, with very large picking uncertainties and without reaching the upper-frequency theoretical array resolution limit.

The Rayleigh wave dispersion curve is retrieved between 2.65 and 16.9 Hz. The uncertainty of the picking is smaller than for the Love waves. The ellipticity angle for the picked Rayleigh wave dispersion curve is positive below about 5.0 Hz, corresponding to prograde particle motion, and negative, indicating retrograde particle motion, at higher frequencies. This change of the sense of rotation indicates a trough in the ellipticity curve at this frequency and is in agreement with the RayDec curve shown in Fig. 4.
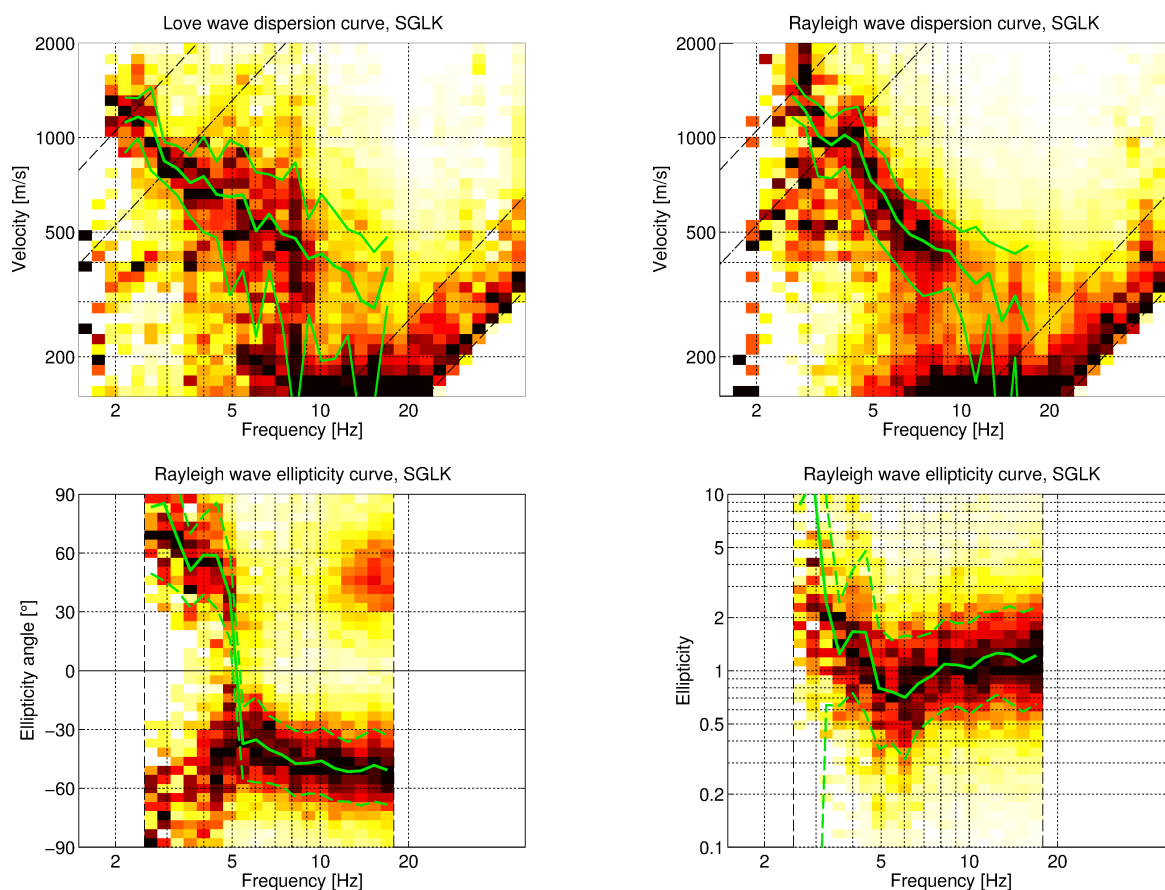

Figure 7: Top: Love (left) and Rayleigh (right) wave dispersion curves obtained with the WaveDec technique (Maranò et al., 2012). The dashed lines indicate the theoretical array resolution limits. Bottom: Rayleigh wave ellipticity angle curve for the picked dispersion curve (left) and Rayleigh wave ellipticity curve, i.e. the absolute value of the tangent of the ellipticity angle.

3.6 SPAC

The SPAC (Aki, 1957) curves of the vertical components have been calculated using the M-SPAC (Bettig et al., 2001) technique implemented in geopsy. Rings with different radius ranges had been defined previously and for all station pairs with distance inside this radius range, the cross-correlation was calculated over a wide frequency range. These cross-correlation curves are averaged for all station pairs of the respective ring and give the SPAC curves. The rings are defined in such a way that at least three station pairs contribute and that their connecting vectors have a good directional coverage. The SPAC curves for all defined rings are shown in Fig. 8. For the smaller rings, the curves are retrieved in the shape of Bessel functions. For the larger rings, which are related with lower frequencies, the retrieved curves are of lower quality. The black points in the curves indicate the data values which contributed to the final dispersion curve estimation, which was made with the function `spac2disp` of the geopsy package. The picked dispersion curve is shown in Fig. 9. It stretches from 3.0 to 9.8 Hz.
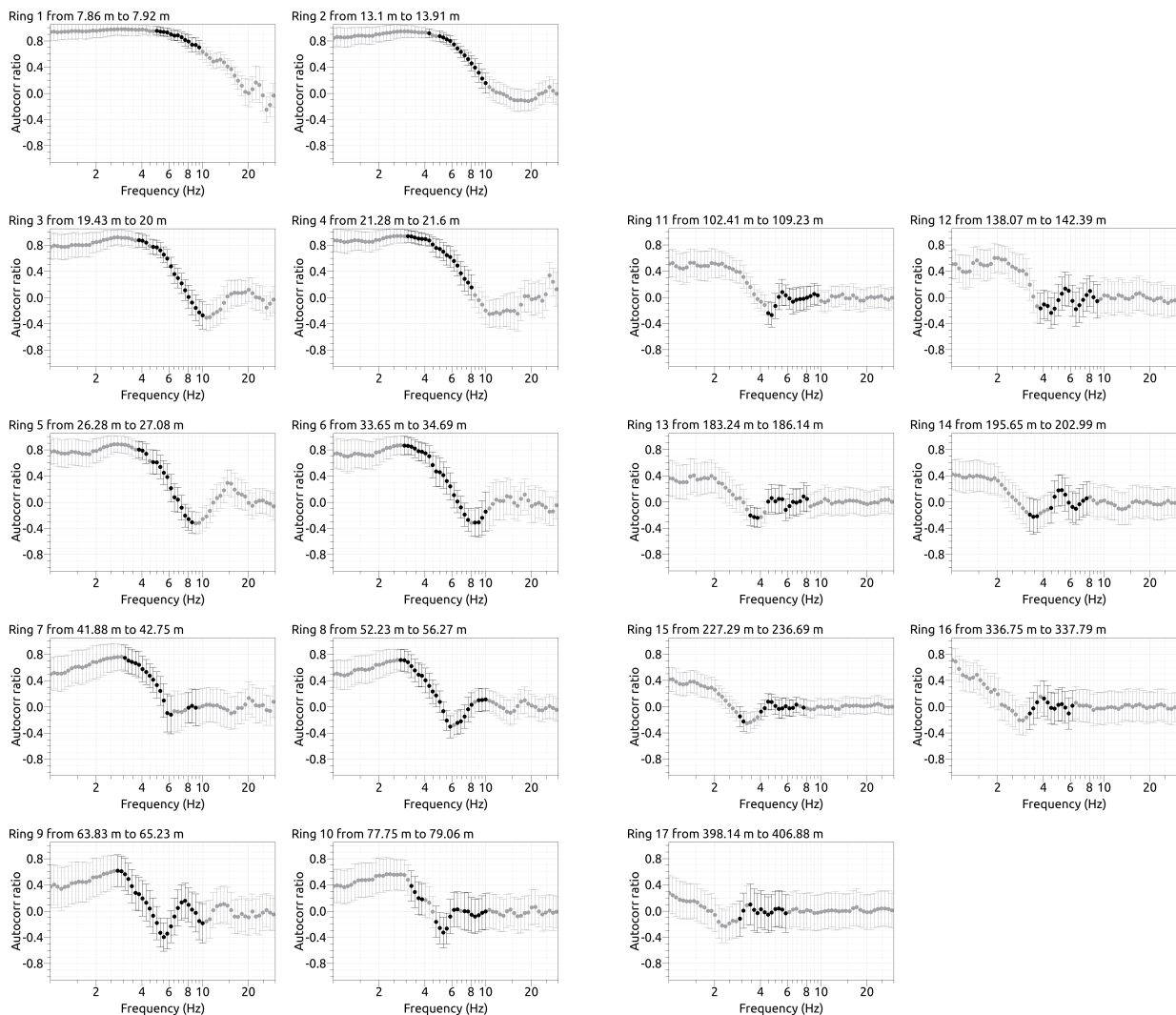
Figure 8: SPAC curves. The black data points contributed to the dispersion curve estimation.
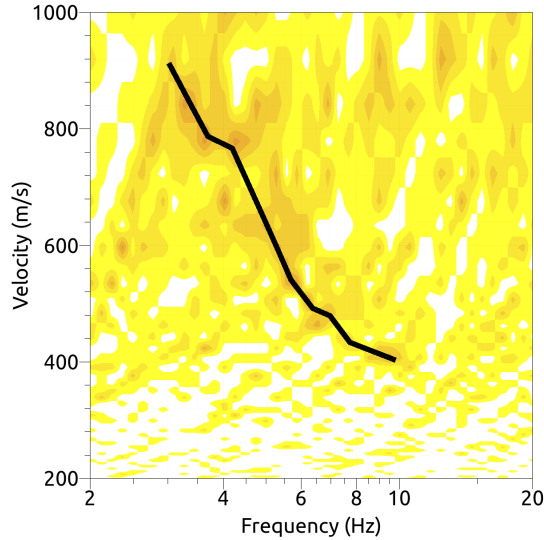
Figure 9: Resulting Rayleigh wave dispersion curve. The black line corresponds to the picked dispersion curve.

3.7 Summary

Fig. 10 gives an overview of the dispersion and ellipticity curves determined by the different methods.

For Love waves, the HRFK and WaveDec results for the respective arrays differ. Between 2 and 3 Hz, they are still in good agreement, but differ more with increasing frequency. The WaveDec curve gives systematically lower velocities than HRKF. In the HRFK plot (Fig. 6), no signs for a mode at the low velocities seen with WaveDec are visible, while in the WaveDec plot (Fig. 7), no dispersion curve is visible where HRFK detects it. Therefore, it is unclear which curve actually corresponds to the fundamental mode and if the HRFK mode might be the first higher mode if the WaveDec curve is the fundamental one. Both curves reach the low-frequency, but not the high-frequency array resolution limit.

For the Rayleigh waves, the different curves differ considerably. SPAC finds the lowest velocities, which are in quite good agreement with the WaveDec curve, even if both techniques diverge below 5 Hz. For HRFK, the vertical and radial dispersion curves agree below 5 Hz and above 10 Hz, but differ considerably in between. This makes the mode attribution difficult. We assume that the SPAC curve would in any case see the fundamental mode or at least a mixture of the fundamental with a higher mode. Therefore, we assume that the WaveDec curve, which is in overall agreement with SPAC, also corresponds to the fundamental mode. The radial HRFK curve is faster than the vertical curve and therefore more different from the WaveDec curve. Therefore, we intrepret the radial curve as belonging to the first higher mode and the vertical one as being a biased estimate between the fundamental and the first higher mode.

The ellipticity curves retrieved using the different methods are in good qualitative agreement. Because of the unclear mode attribution, we will disregard the HRFK ellipticity estimates. Using WaveDec, frequencies below 2.65 Hz are not retrieved. At around 2.4 Hz, the ellipticity peak was identified using RayDec. The WaveDec curve is retrograde above 5 Hz and prograde below. This coincides with the trough observed by RayDec between 5 and 6 Hz. We identify this trough as belonging to a singularity. Consequently, as the fundamental mode Rayleigh wave must be retrograde at low freuqencies, we identify the ellipticity peak as related with a singularity as well, even if it is not extremely pronounced with RayDec.

For the dispersion curves, a second hypothesis would consist in trusting the HRFK curves more than the others. According to this hypothesis, the observed dispersion curves of the transverse and vertical components would correspond to the fundamental modes of Love and Rayleigh waves, respectively.
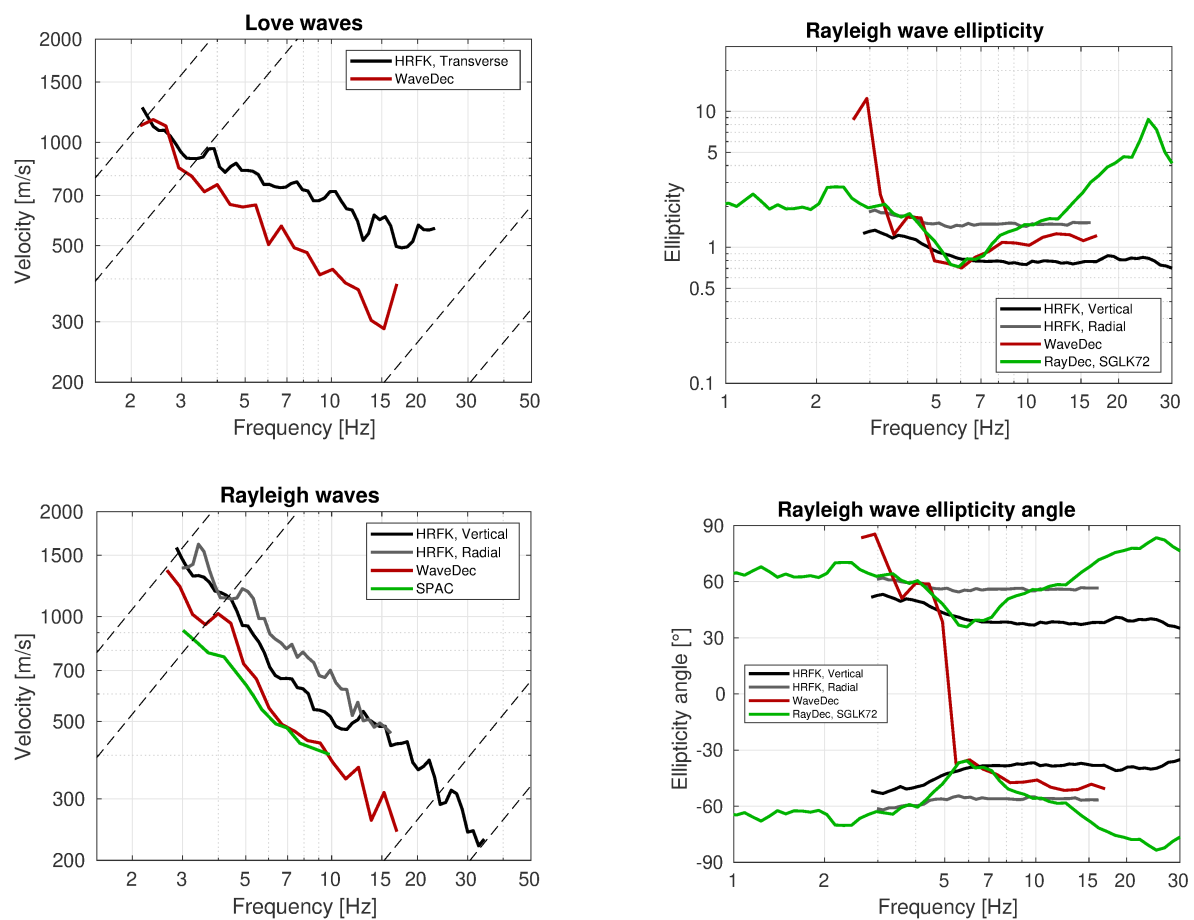

Figure 10: Overview of the Love and Rayleigh wave dispersion curves as well as the ellipticity and ellipticity angle curves for both arrays. The dashed lines indicate the theoretical resolution limits of the array. The RayDec ellipticity curve corresponds to station SGLK72.

4 Data inversion

4.1 Inversion targets

We performed inversions using two different targets, as interpreted above. The first target (see Table 1) uses the WaveDec Love and Rayleigh wave dispersion curves as respective fundamental modes. Additionally, the transverse HRFK curve above 6.2 Hz is used as first higher mode. For Rayleigh waves, the radial HRFK curve is used as first higher mode. For the ellipticity angle, the WaveDec curve was used above 2.97 Hz and a part of the RayDec curve below, assuming retrograde particle motion, in order to force the inversion to find a singularity at this frequency.
For the second target (see Table 2), the transverse HRFK dispersion curve was used as fundamental Love wave mode and the vertical HRFK curve as fundamental Rayleigh wave mode. No higher modes are used in this case.
The inversion targets are shown in Fig. 11.

4.2 Inversion parameterization

For each target, six different parameterizations have been used in total. The first five had free values of the depths and velocities of the different layers, ranging from four to eight layers (including half-space). The last parameterization had fixed layer depths and consisted of 20 layers in total. The P-wave velocities were allowed to vary up to $5000 \, m/s$. The S-wave velocities were allowed to range from 30 to $3500 \, m/s$. The deepest layers were parameterized to range to a depth of $200 \, m$ maximum. The density was fixed to $2\,300 \, kg/m^3$ for the lowest layer, to $1\,900 \, kg/m^3$ for the superficial layer (or the first three layers in the fixed-layer case) and to $2\,100 \, kg/m^3$ for all other layers. No low-velocity zones were allowed.

Table 1: List of the different data curves used as target 1 in the different inversions.

Method	Wave type	Mode	Curve type	Frequency range [Hz]
WaveDec	Love	fundamental	dispersion	2.20 - 15.3
HRFK (T)	Love	first harmonic	dispersion	6.24 - 22.7
WaveDec	Rayleigh	fundamental	dispersion	2.69 - 16.9
HRFK (R)	Rayleigh	first harmonic	dispersion	3.12 - 16.1
RayDec (SGLK72)	Rayleigh	fundamental	ellipticity angle	2.00 - 2.11
WaveDec	Rayleigh	fundamental	ellipticity angle	2.97 - 16.9

Table 2: List of the different data curves used as target 2 in the different inversions.

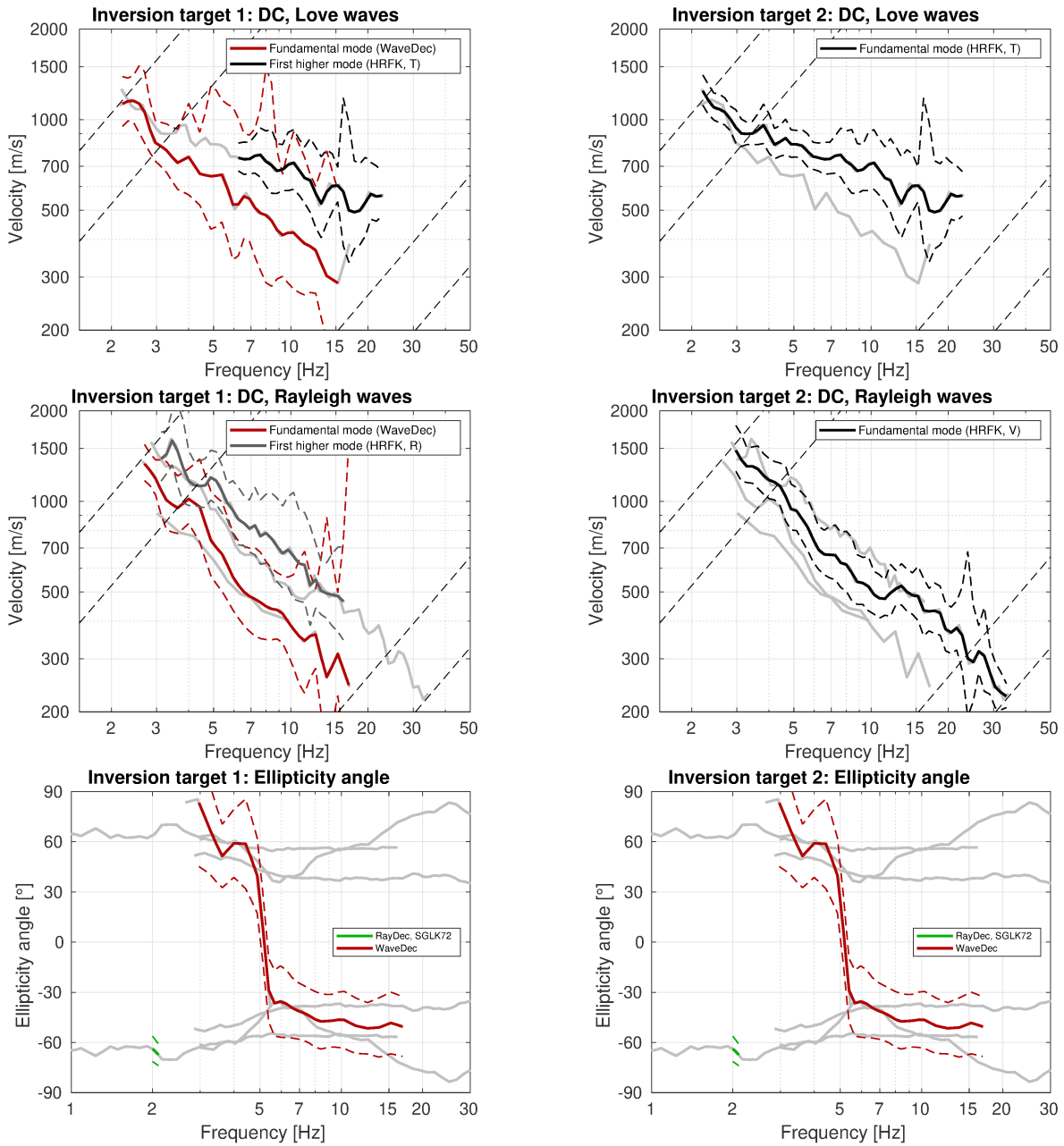| Method	Wave type	Mode	Curve type	Frequency range [Hz]
HRFK (T)	Love	fundamental	dispersion	2.20 - 22.7
HRFK (V)	Rayleigh	fundamental	dispersion	2.97 - 33.7
RayDec (SGLK72)	Rayleigh	fundamental	ellipticity angle	2.00 - 2.11
WaveDec	Rayleigh	fundamental	ellipticity angle	2.97 - 16.9

Figure 11: Overview of the Love (top) and Rayleigh (center) wave dispersion and ellipticity angle (bottom) curves used as targets 1 (left) and 2 (right) for the different inversions.

4.3 Inversion results

We performed six inversions with different parameterizations for both targets. In Table 3, the obtained minimum misfit values for these inversions are shown. Each inversion run produced around 150 000 total models in order to assure a good convergence of the solution, except for the 4-layer inversion, where 100 000 generated models were sufficient. The results of the inversions SGLK4l1 - SGLKfix1 (target 1) are shown in Figs 12 - 17 and in Figs 18 - 23 for SGLK4l2 - SGLKfix2 (target 2).

The different inversions for each target yield similar misfit values and fit the data in a comparable way. The 4-layer inversions yield slightly higher misfit values than the 5-, 6-, 7- and 8-layer inversions. Using the fixed-depth approach, the minimum misfit was also higher, probably because the interface depths were fixed at non-optimum depths.

It is surprising that the minimum misfit for target 1 is actually lower than for target 2, although more curves and more modes are inverted here. The four dispersion curves are all fitted. For the Love wave first higher mode, there is some discrepancy at the low-frequency limit, but this can be expected as the fundamental model is getting close there. The three other modes and the ellipticity angle are fitted very well. For target 2, the Love and Rayleigh wave dispersion curves are fitted, but some larger differences between the generated models and the measured curves are visible.

Table 3: List of inversions

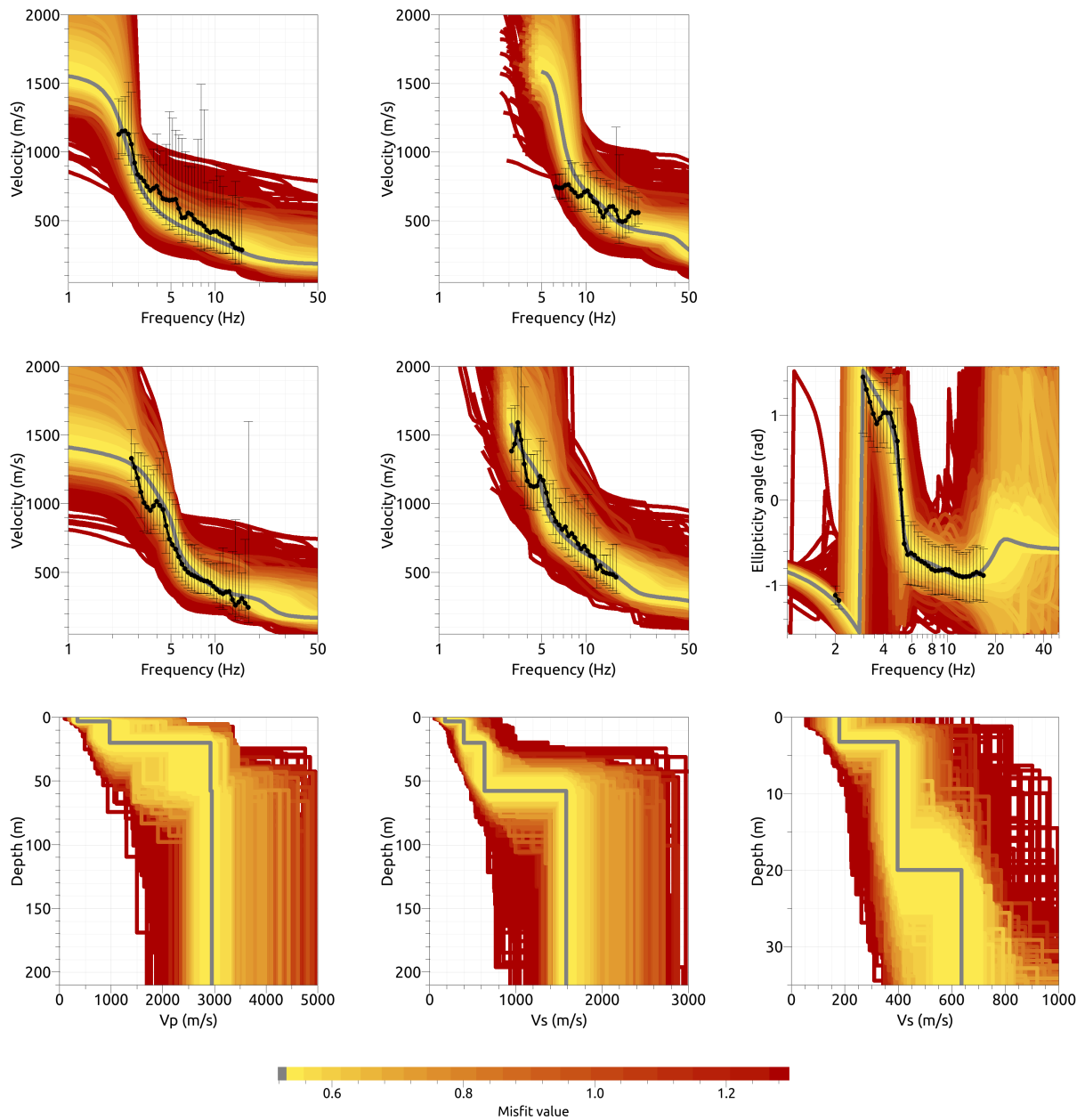| Target	Inversion	Number of layers	Number of models	Minimum misfit
1	SGLK4l1	4	100 027	0.531
1	SGLK5l1	5	150 030	0.515
1	SGLK6l1	6	150 016	0.516
1	SGLK7l1	7	150 040	0.518
1	SGLK8l1	8	150 026	0.524
1	SGLKfix1	20	150 041	0.553
2	SGLK4l2	4	100 012	0.623
2	SGLK5l2	5	150 017	0.609
2	SGLK6l2	6	150 010	0.603
2	SGLK7l2	7	150 037	0.603
2	SGLK8l2	8	150 081	0.605
2	SGLKfix2	20	150 024	0.676

Figure 12: Inversion SGLK4l1. Top line: Dispersion curves for the fundamental mode (left) and the first higher mode (center) of Love waves. Center line: Dispersion curves for the fundamental mode (left) and the first higher mode (center) of Rayleigh waves and ellipticity angle of the fundamental mode (right). Bottom line: P-wave velocity profiles (left), S-wave velocity profiles (center and zoom on the upper 50 m on the right). The black dots indicate the data points used for the inversion, the gray line indicates the best-fitting model.
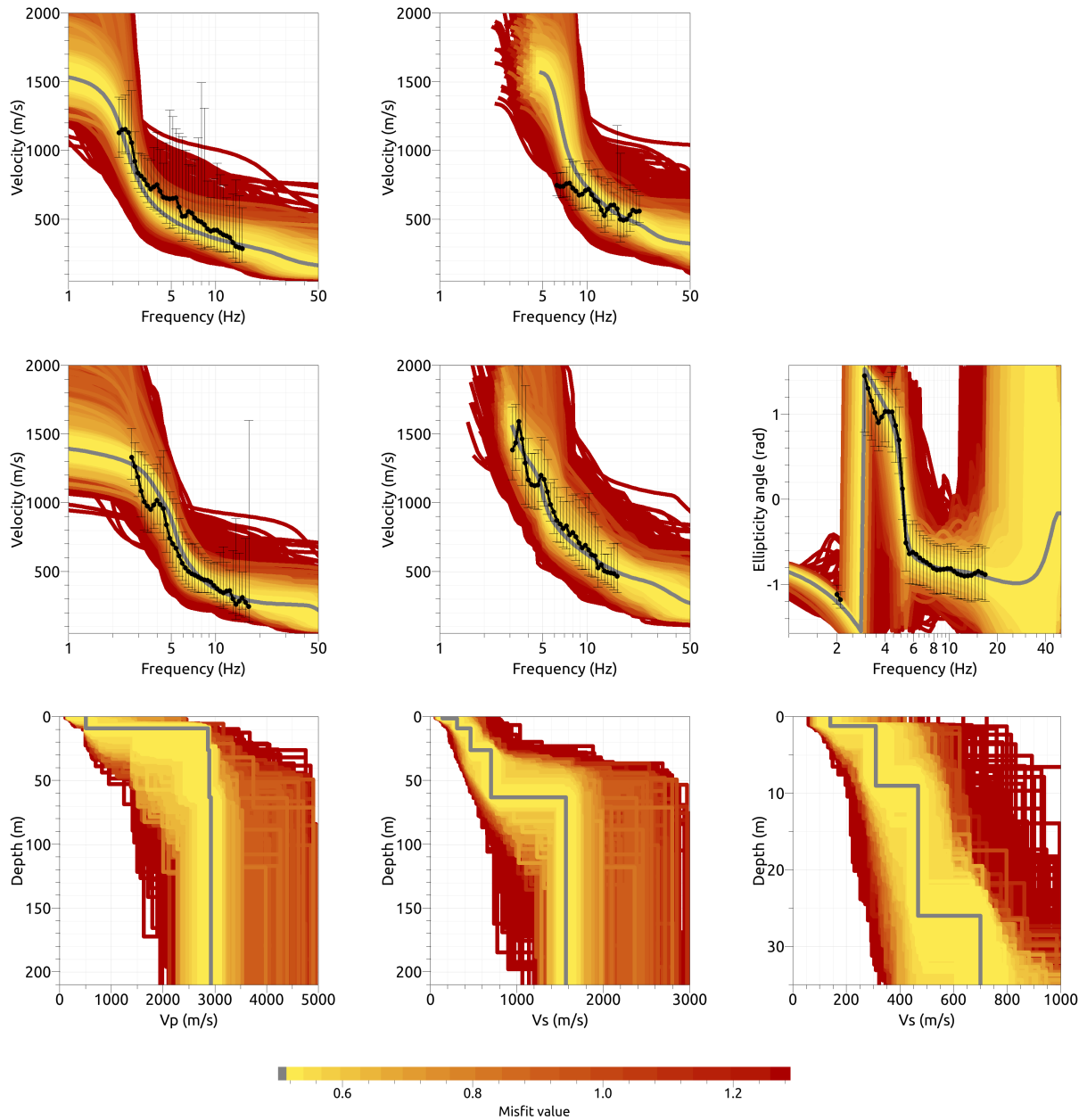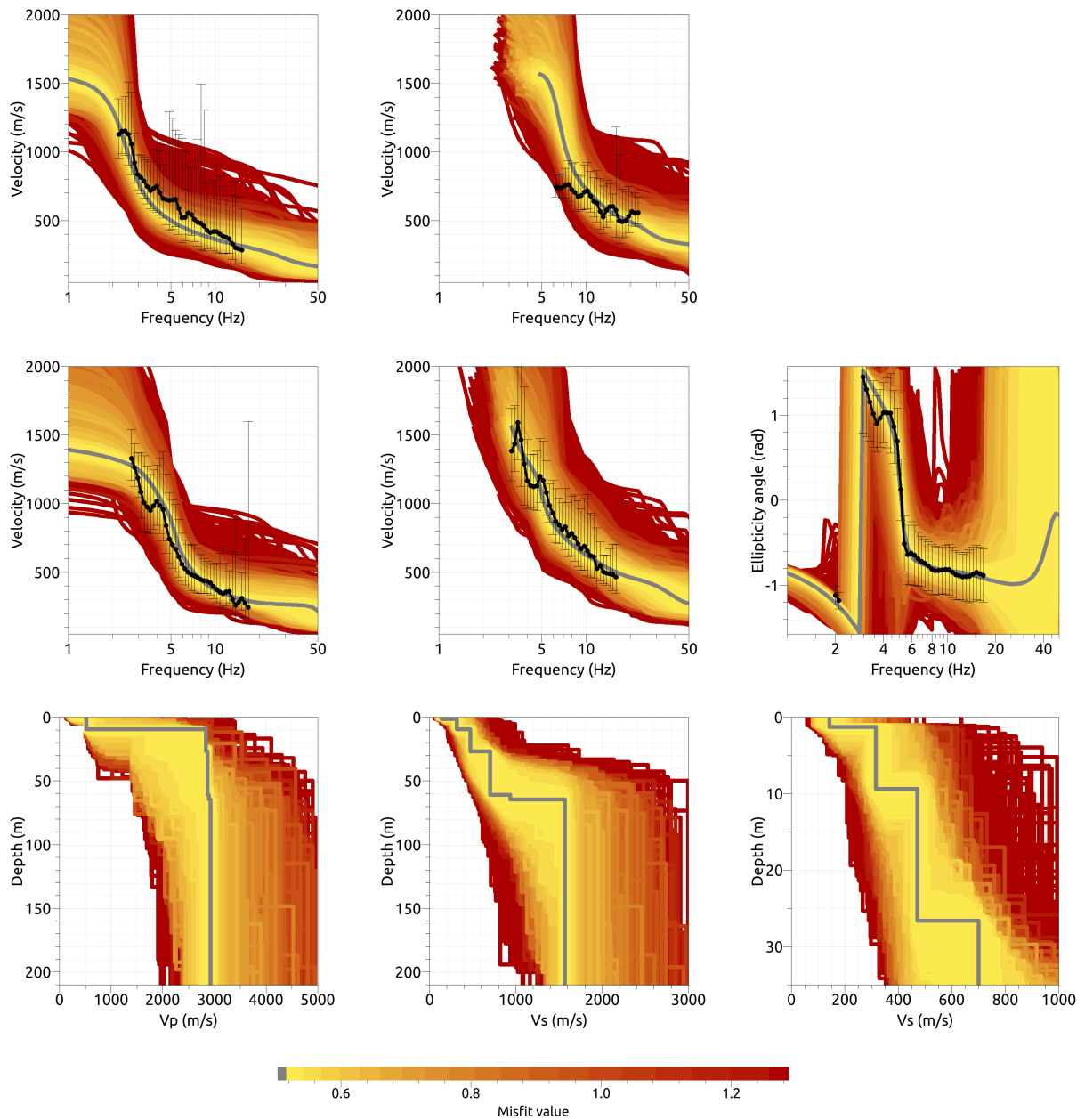
Figure 13: Inversion SGLK5l1. Top line: Dispersion curves for the fundamental mode (left) and the first higher mode (center) of Love waves. Center line: Dispersion curves for the fundamental mode (left) and the first higher mode (center) of Rayleigh waves and ellipticity angle of the fundamental mode (right). Bottom line: P-wave velocity profiles (left), S-wave velocity profiles (center and zoom on the upper 50 m on the right). The black dots indicate the data points used for the inversion, the gray line indicates the best-fitting model.

Figure 14: Inversion SGLK6l1. Top line: Dispersion curves for the fundamental mode (left) and the first higher mode (center) of Love waves. Center line: Dispersion curves for the fundamental mode (left) and the first higher mode (center) of Rayleigh waves and ellipticity angle of the fundamental mode (right). Bottom line: P-wave velocity profiles (left), S-wave velocity profiles (center and zoom on the upper 50 m on the right). The black dots indicate the data points used for the inversion, the gray line indicates the best-fitting model.
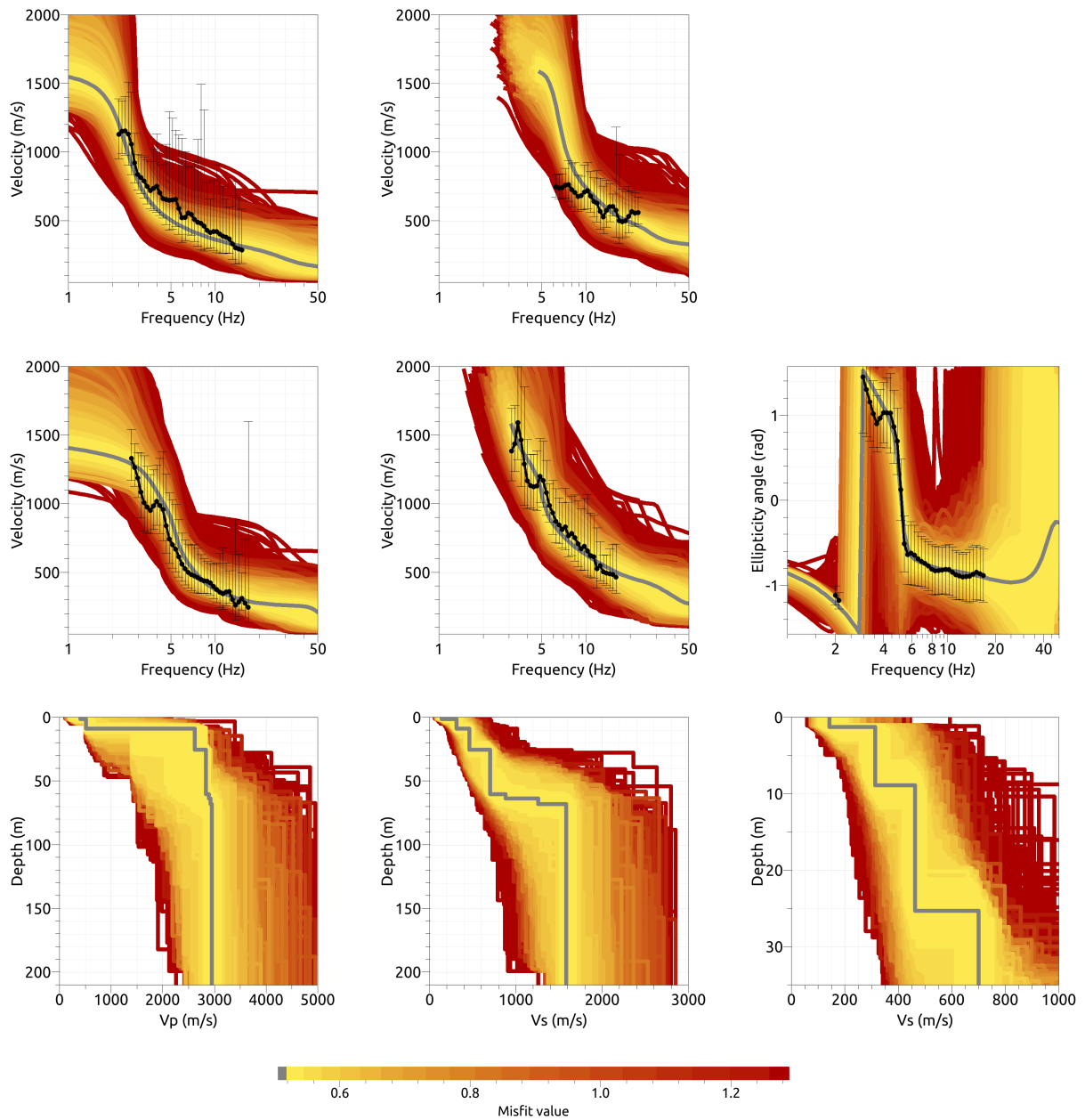
Figure 15: Inversion SGLK7l1. Top line: Dispersion curves for the fundamental mode (left) and the first higher mode (center) of Love waves. Center line: Dispersion curves for the fundamental mode (left) and the first higher mode (center) of Rayleigh waves and ellipticity angle of the fundamental mode (right). Bottom line: P-wave velocity profiles (left), S-wave velocity profiles (center and zoom on the upper 50 m on the right). The black dots indicate the data points used for the inversion, the gray line indicates the best-fitting model.
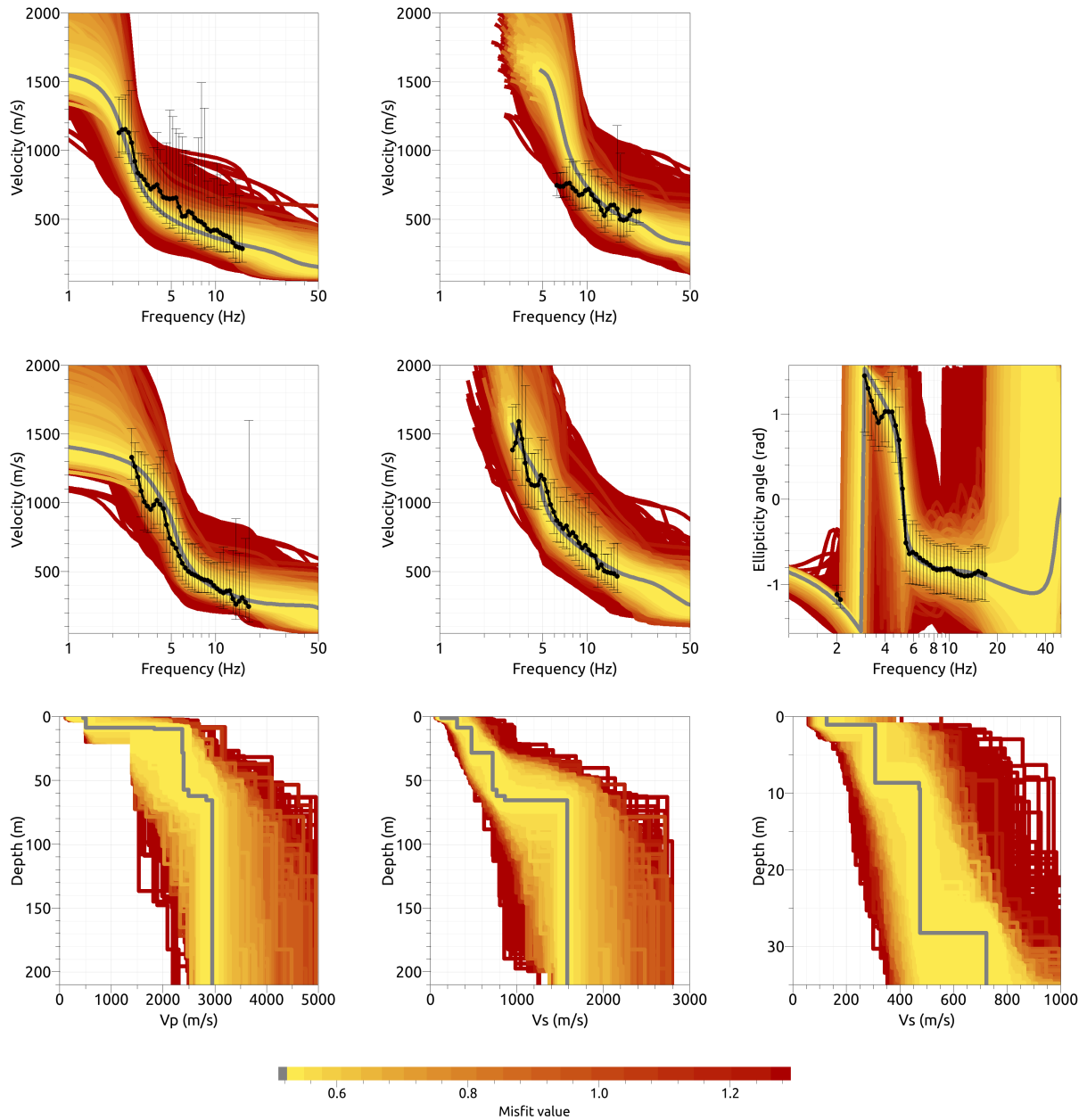
Figure 16: Inversion SGLK8l1. Top line: Dispersion curves for the fundamental mode (left) and the first higher mode (center) of Love waves. Center line: Dispersion curves for the fundamental mode (left) and the first higher mode (center) of Rayleigh waves and ellipticity angle of the fundamental mode (right). Bottom line: P-wave velocity profiles (left), S-wave velocity profiles (center and zoom on the upper 50 m on the right). The black dots indicate the data points used for the inversion, the gray line indicates the best-fitting model.
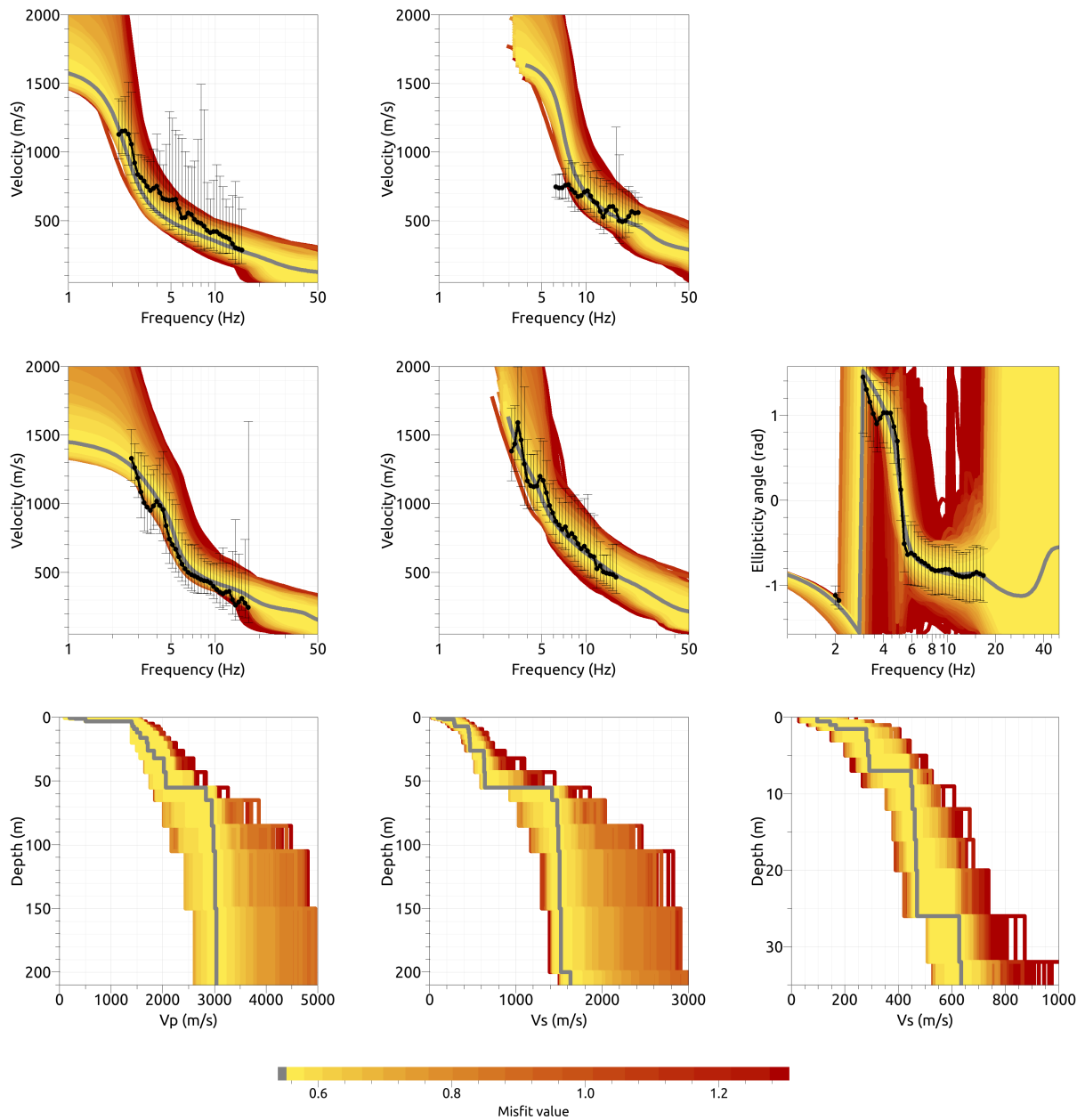
Figure 17: Inversion SGLKfix1. Top line: Dispersion curves for the fundamental mode (left) and the first higher mode (center) of Love waves. Center line: Dispersion curves for the fundamental mode (left) and the first higher mode (center) of Rayleigh waves and ellipticity angle of the fundamental mode (right). Bottom line: P-wave velocity profiles (left), S-wave velocity profiles (center and zoom on the upper 50 m on the right). The black dots indicate the data points used for the inversion, the gray line indicates the best-fitting model.
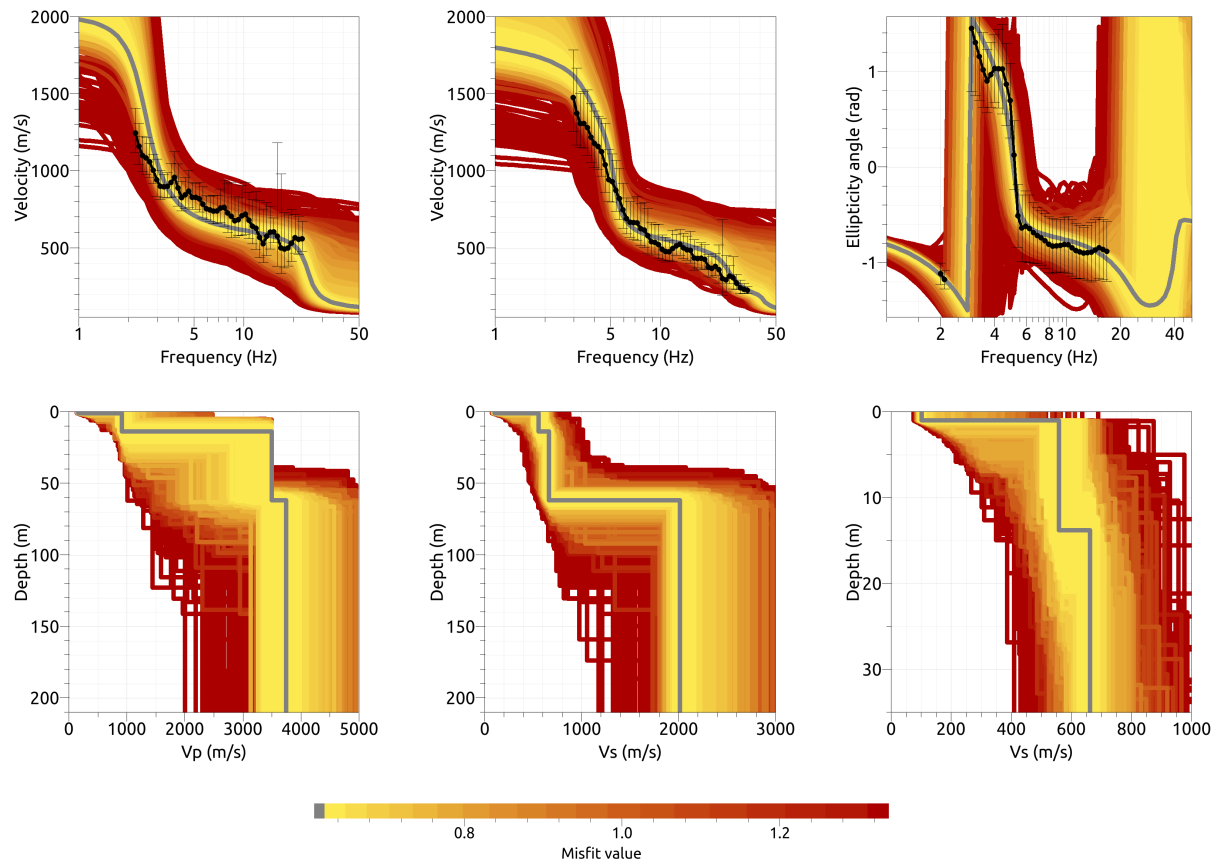
Figure 18: Inversion SGLK4l2. Top line: Dispersion curves for Love waves (left) and Rayleigh waves (center) and Rayleigh wave ellipticity angle (right) of the respective fundamental modes. Bottom line: P-wave velocity profiles (left), S-wave velocity profiles (center and zoom on the upper 50 m on the right). The black dots indicate the data points used for the inversion, the gray line indicates the best-fitting model.
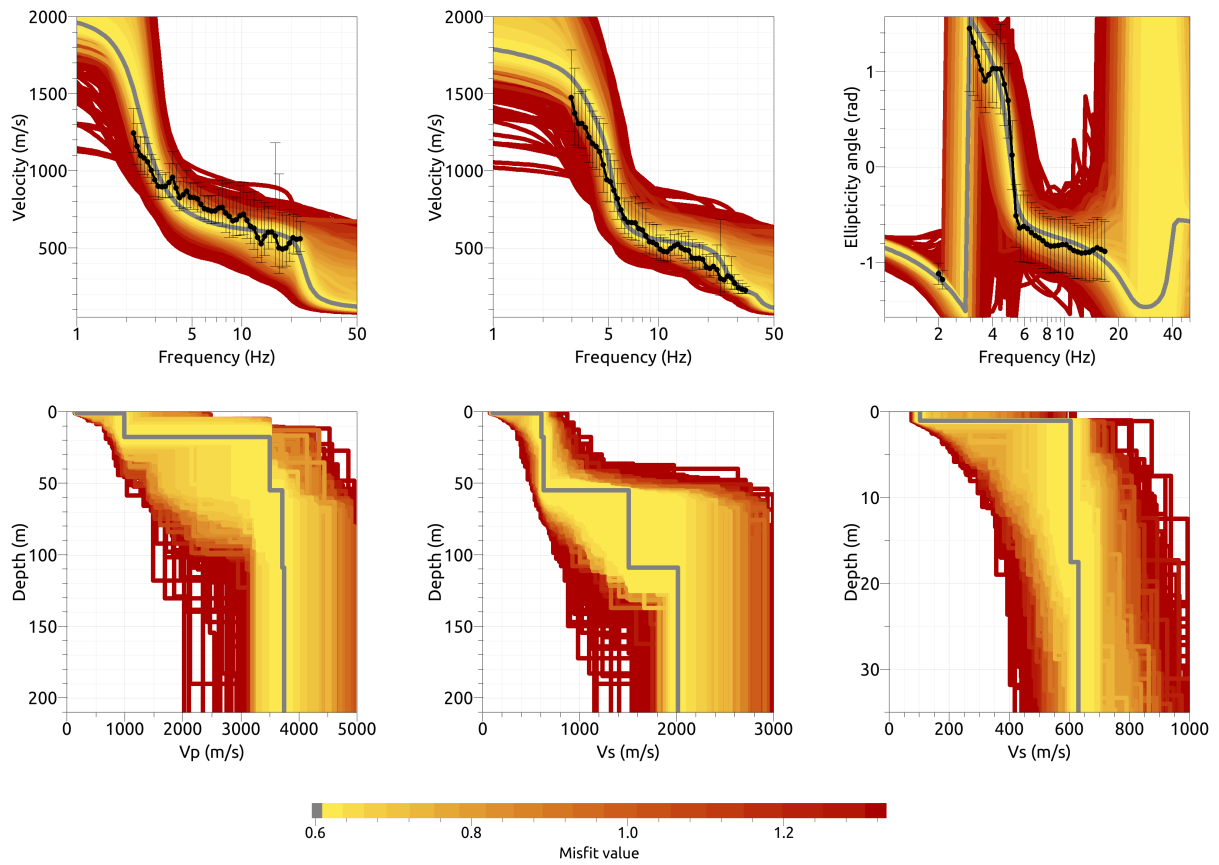
Figure 19: Inversion SGLK5l2. Top line: Dispersion curves for Love waves (left) and Rayleigh waves (center) and Rayleigh wave ellipticity angle (right) of the respective fundamental modes. Bottom line: P-wave velocity profiles (left), S-wave velocity profiles (center and zoom on the upper 50 m on the right). The black dots indicate the data points used for the inversion, the gray line indicates the best-fitting model.

Figure 20: Inversion SGLK6l2. Top line: Dispersion curves for Love waves (left) and Rayleigh waves (center) and Rayleigh wave ellipticity angle (right) of the respective fundamental modes. Bottom line: P-wave velocity profiles (left), S-wave velocity profiles (center and zoom on the upper 50 m on the right). The black dots indicate the data points used for the inversion, the gray line indicates the best-fitting model.
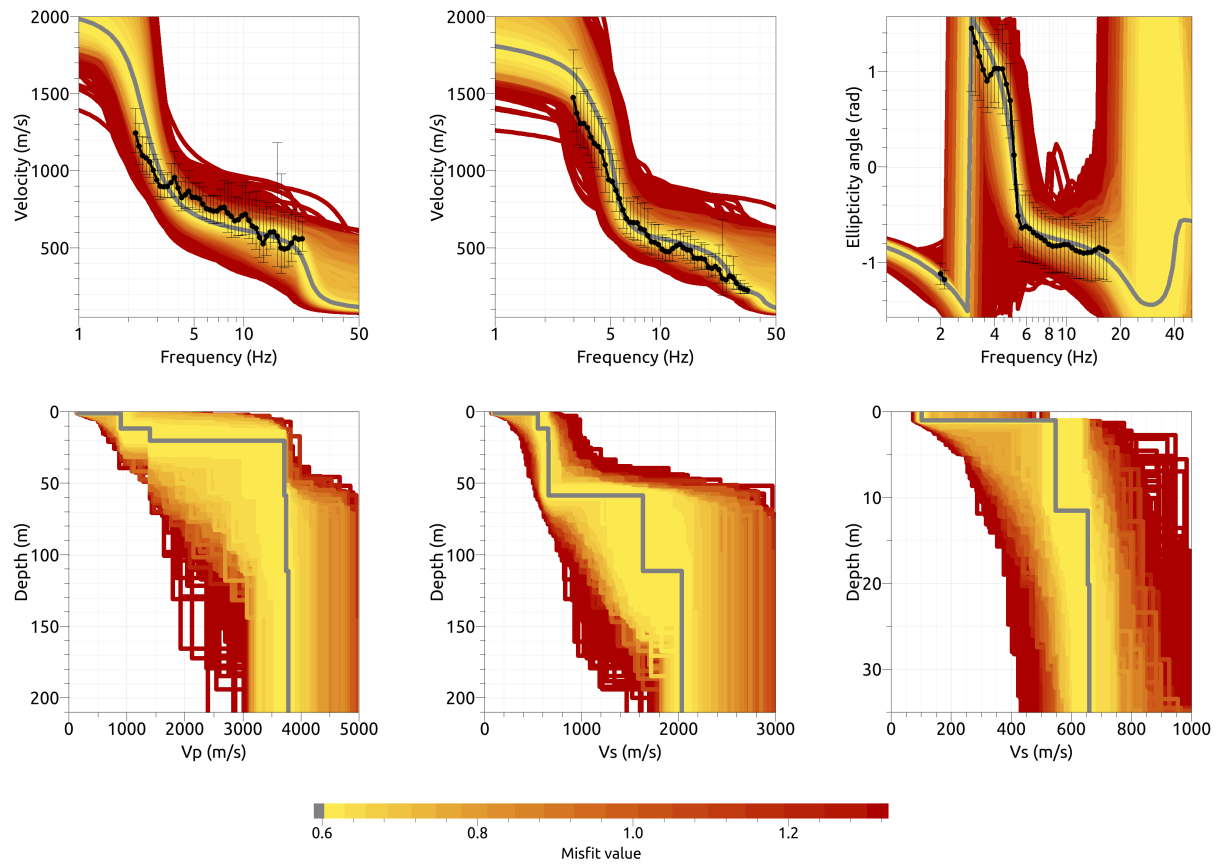
Figure 21: Inversion SGLK7l2. Top line: Dispersion curves for Love waves (left) and Rayleigh waves (center) and Rayleigh wave ellipticity angle (right) of the respective fundamental modes. Bottom line: P-wave velocity profiles (left), S-wave velocity profiles (center and zoom on the upper 50 m on the right). The black dots indicate the data points used for the inversion, the gray line indicates the best-fitting model.
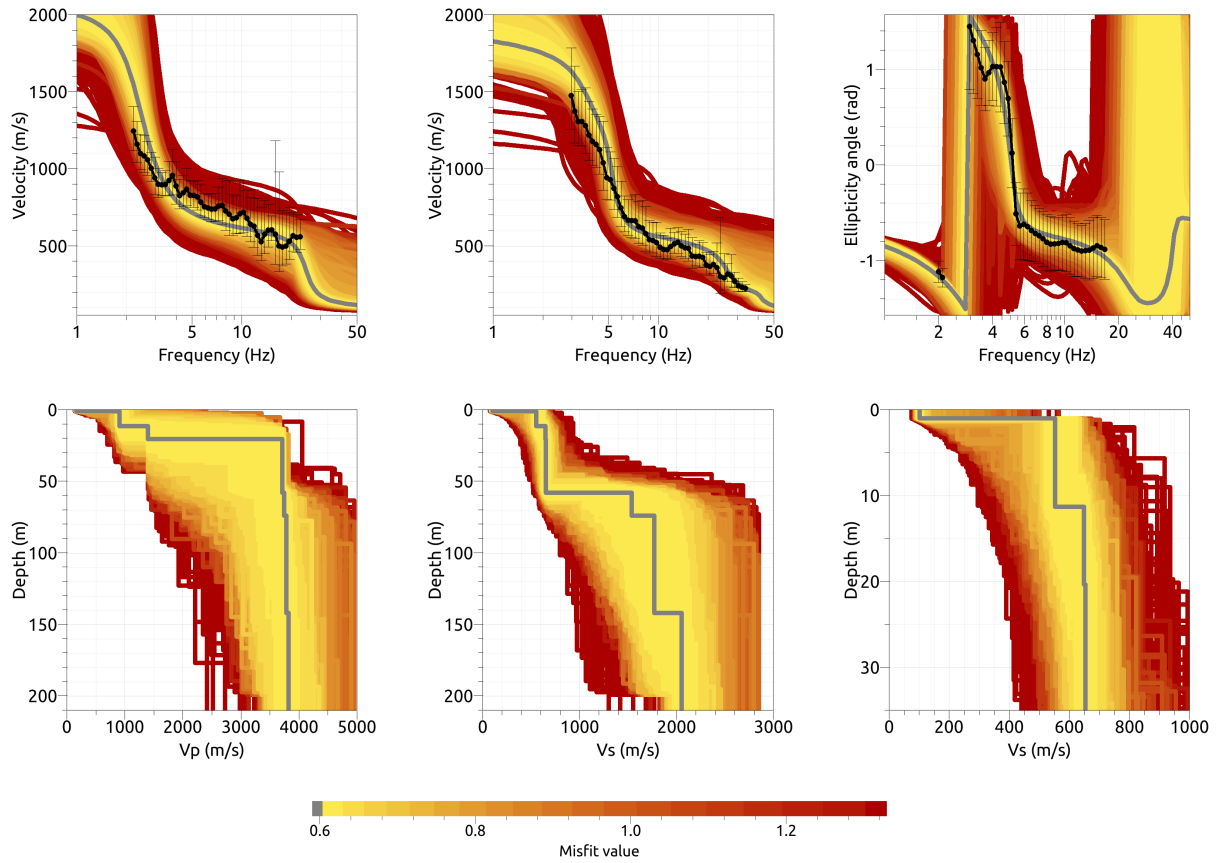
Figure 22: Inversion SGLK8l2. Top line: Dispersion curves for Love waves (left) and Rayleigh waves (center) and Rayleigh wave ellipticity angle (right) of the respective fundamental modes. Bottom line: P-wave velocity profiles (left), S-wave velocity profiles (center and zoom on the upper 50 m on the right). The black dots indicate the data points used for the inversion, the gray line indicates the best-fitting model.
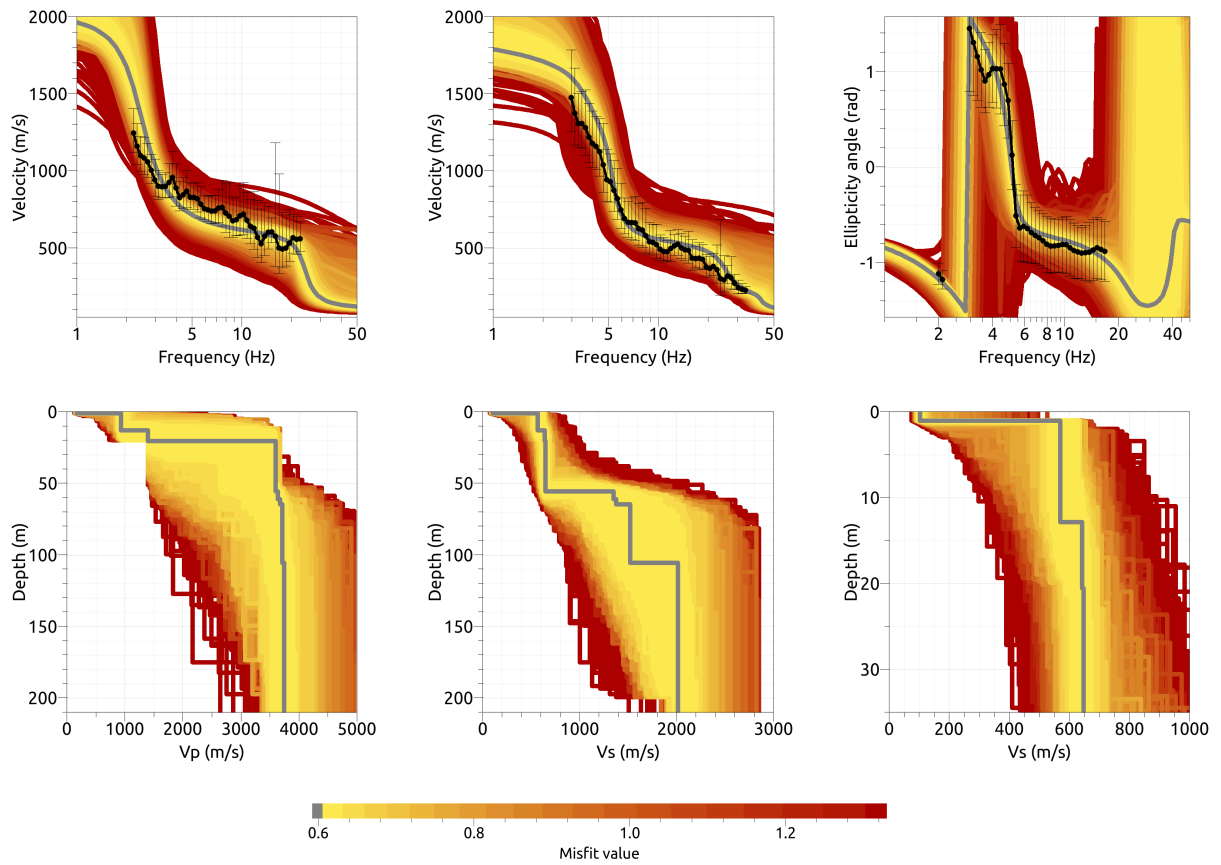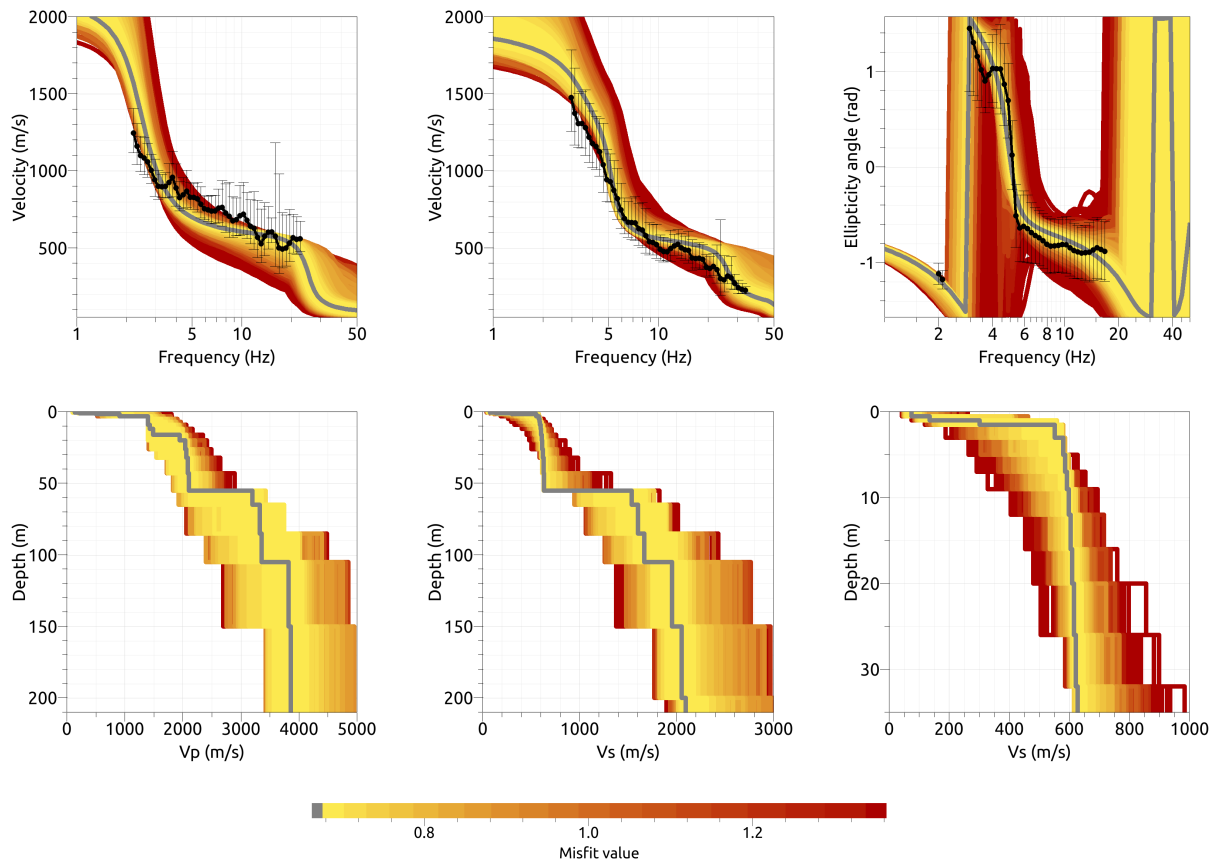
Figure 23: Inversion SGLKfix2. Top line: Dispersion curves for Love waves (left) and Rayleigh waves (center) and Rayleigh wave ellipticity angle (right) of the respective fundamental modes. Bottom line: P-wave velocity profiles (left), S-wave velocity profiles (center and zoom on the upper 50 m on the right). The black dots indicate the data points used for the inversion, the gray line indicates the best-fitting model.

4.4 Overview of the inversion result

The best-fitting models of all inversions are shown in Fig. 24. As the data used for target 1 and target 2 have a different mode attribution, the resulting velocity profiles are also very different, especially in the surficial 30 m.

For target 1, the best model for inversion SGLK4l1 differs considerably from the others because it does not have enough complexity to model the structure as detailed as the other models, even if the misfit is not much higher than for the other cases. For the overview, we will not consider this model any more. The models SGLK5l1-SGLKfix1 are in quite good overall agreement. They show a shallow layer with shear-wave velocity between 95 and 150 m/s with a thickness of about 1 to 1.5 m, followed by a layer with a velocity between 300 and 320 m/s down to about 8.5-9.5 m of depth. The velocity increases to about 460-480 m/s down to a depth of about 25 to 29 m. Here, the velocity increases to values between 625 and 725 m/s. The seismic bedrock is found in a depth of around 60-66 m, where the velocity increases to over 1500 m/s. In the fixed-depth approach, the velocity contrasts are in general smoother with more signs of a velocity gradient, but the overall trend is similar, even if the bedrock depth is found at 55 m in this case.

For target 2, the velocities are in general faster. A shallow layer with a thickness of 1 m and a shear-wave velocity of about 100 m/s is found for all models, followed by a layer with a velocity between 545 and 605 m/s reaching to a depth of around 11.5-14 m. Here, the velocity increases to about 630-665 m/s. The seismic bedrock is found at depths between 55 and 62 m.

The V_{S30} values for the inversions using target 1 range from 383.8 to 398.7 m/s (average value $393.9 \pm 5.4 \, m/s$). For target 2, the V_{S30} values range from 505.8 to 525.6 m/s (average value $521.8 \pm 7.9 \, m/s$). For target 1, this corresponds to soil class B in EC8 and C in SIA261. For target 2, this corresponds to soil class B in both EC8 and SIA261.
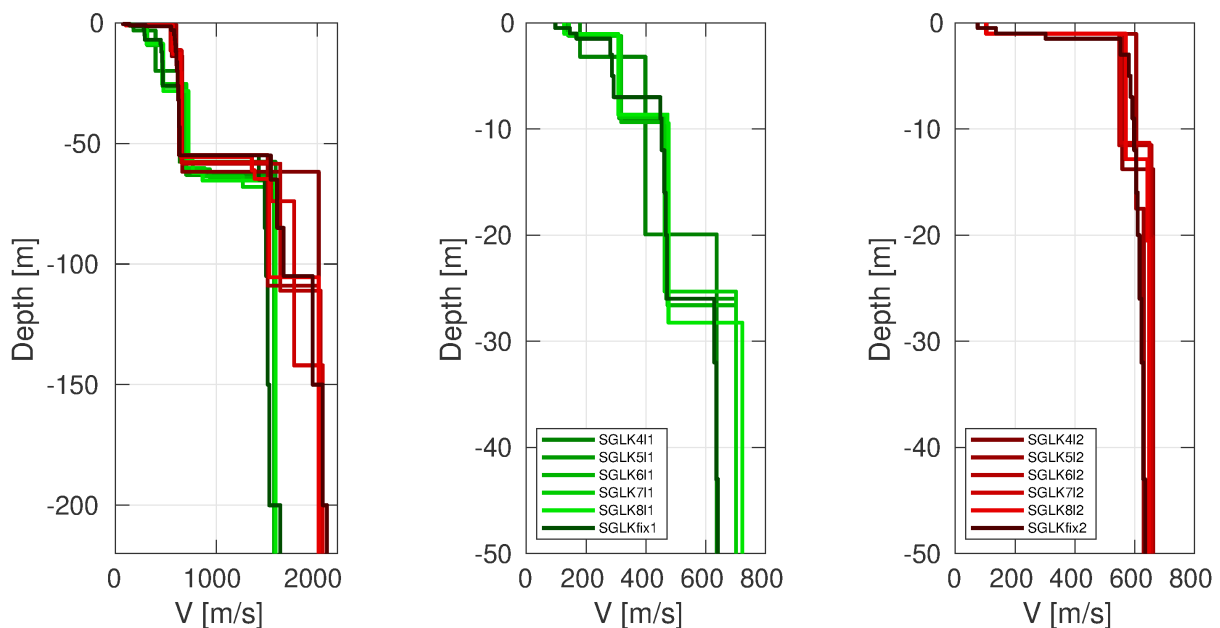

Figure 24: Overview of shear-wave velocity profiles of the best-fitting models of all inversions (left) and a zoom on the shallow part for the inversions using target 1 (center) and target 2 (right).

4.5 Amplification function

In Fig. 25, the theoretical amplification function for the best models resulting from the inversions is compared with the empirical amplification of station SGLK, based on 11 events so far. The empirical amplification shows a first peak at around 1.2 Hz with an amplification not exceeding 3, followed by a range with amplification values between 1.6 and 3.1 up to about 7 Hz. No pronounced amplification peaks are visible. This might be caused by edge-generated surface waves in the basin.

The models resulting from the inversions show an amplification peak at around 2.6 Hz in both cases, followed by several peaks and troughs. Edge-generated surface waves are not taken into account in this modeling. Overall, the amplification function for the models of target 1 is closer to the empirical amplification of the site. As these models also seem more reasonable, we choose the results of the inversion with target 1 as representative results for the site.
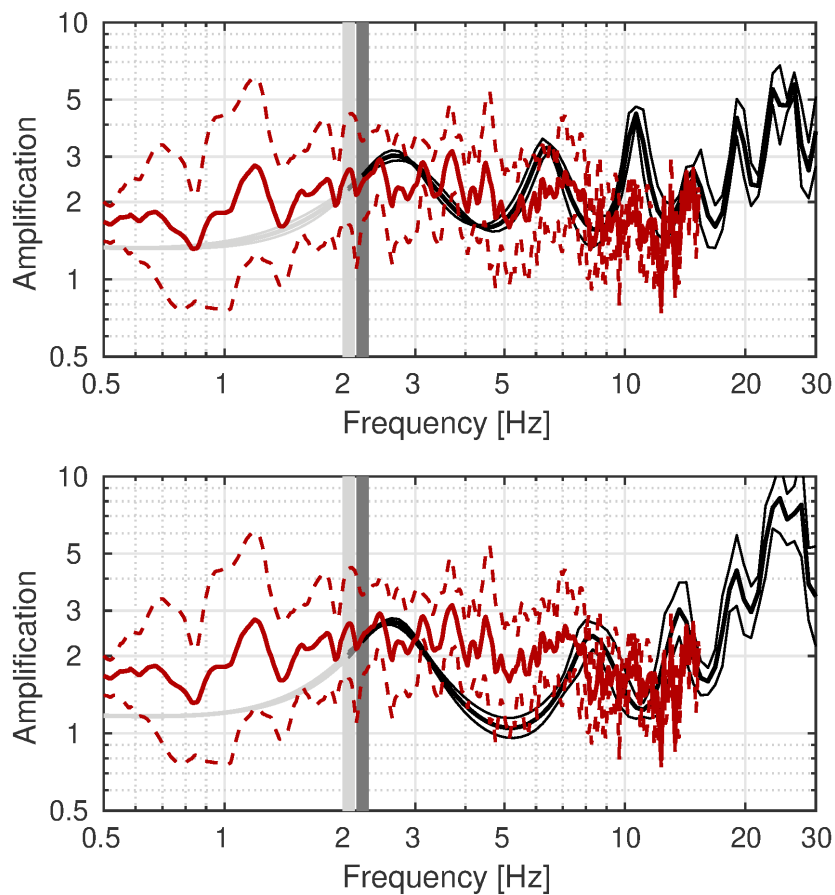

Figure 25: Comparison between the modeled amplification for the final set of best models of the different inversions (in grey to black, with standard deviation) and the empirical amplification measured at station SGLK (red, with standard deviation) for target 1 (top) and target 2(bottom). The vertical light and dark grey bars correspond to the lowest frequency of the ellipticity and dispersion curves used for the inversion, respectively.

4.6 Quarter-wavelength representation

The quarter-wavelength velocity approach (Joyner et al., 1981) provides, for a given frequency, the average velocity at a depth corresponding to 1/4 of the wavelength of interest. It is useful to identify the frequency limits of the experimental data (the minimum frequency of the dispersion curve used in the inversion is 2.2 Hz for both targets, the minimum frequency used for the ellipticity inversion 2.00 Hz). The results using this proxy show that the dispersion curves constrain the profiles down to about 62 m for target 1 and 92 m for target 2 (Fig. 26). Moreover, the quarter wavelength impedance-contrast introduced by Poggi et al. (2012) is also displayed in the figure. It corresponds to the ratio between two quarter-wavelength average velocities, respectively from the top and the bottom part of the velocity profile, at a given frequency (Poggi et al., 2012). This curve shows a strong contrast at the fundamental frequency of the site.
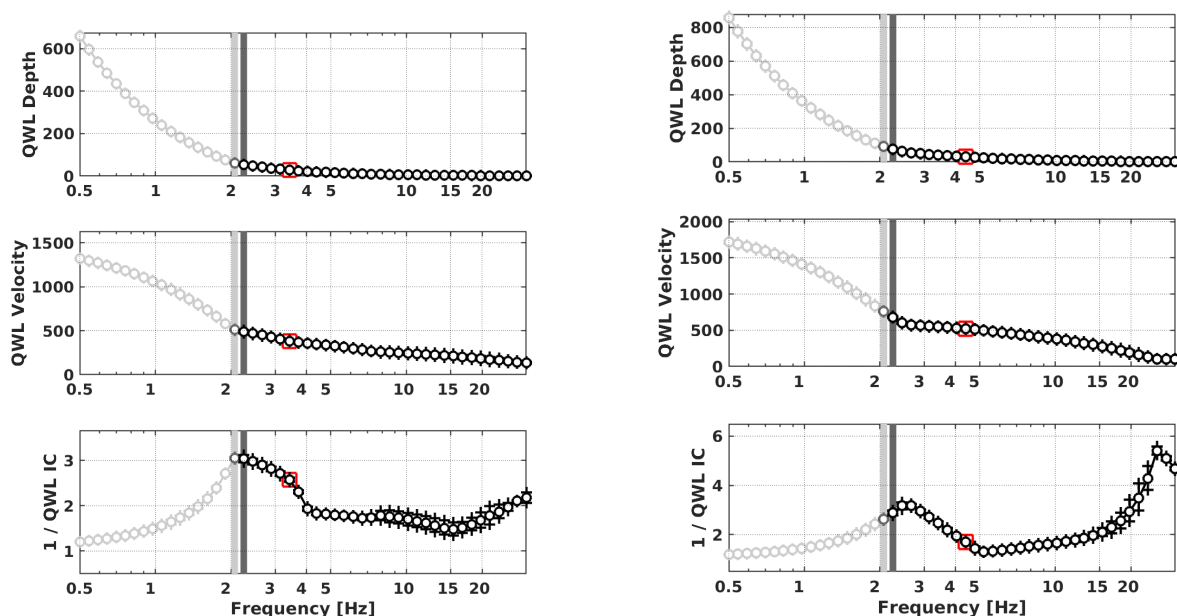

Figure 26: Quarter wavelength representation of the velocity profile for the best models of the inversions (top: depth, center: velocity, bottom: inverse of the impedance contrast) for the resulting models of target 1 (left) and target 2 (right). The black curves are constrained by the dispersion curves, the light grey curves are not constrained by the data. The red square corresponds to V_{S30}.

5 Conclusion

We performed a passive array measurement to characterize the soil underneath station SGLK in Glarus. According to the geological atlas, the station is located on river gravels. The dispersion curves for Love and Rayleigh waves could be measured with several methods, but the results of the different methods were not compatible assuming the same mode attribution. Therefore, the final interpretation is that WaveDec and SPAC retrieved the dispersion curves for the fundamental Love and Rayleigh wave modes, while HRFK retrieved the first higher modes in both cases. In the H/V and ellipticity curves, a first, broad peak is found around 1 Hz and a more pronounced peak at around 2.4 Hz, which, according to the WaveDec measurements, corresponds to a singularity. The inversion of target 1, corresponding to the preferred interpretation of the measurements including the fundamental and first higher modes for Love and Rayleigh waves and the ellipticity angle information, shows a structure with major interfaces at around 1 m, 9 m, 27 m and 60 m, with a V_{S30} of about 394 m/s, corresponding to soil class B in EC8 and C in SIA261.

Acknowledgements

References

Aki, K. (1957). Space and time spectra of stationary stochastic waves, with special reference to microtremors. *Bull. Earthquake Res. Inst. Tokyo Univ.*, 35:415–456.

Bettig, B., Bard, P.-Y., Scherbaum, F., Riepl, J., Cotton, F., Cornou, C., and Hatzfeld, D. (2001). Analysis of dense array noise measurements using the modified spatial auto-correlation method (SPAC): application to the Grenoble area. *Boll. Geof. Teor. Appl.*, 42:281–304.

Burjánek, J., Gassner-Stamm, G., Poggi, V., Moore, J. R., and Fäh, D. (2010). Ambient vibration analysis of an unstable mountain slope. *Geophys. J. Int.*, 180:820–828.

Burjánek, J., Moore, J. R., Molina, F. X. Y., and Fäh, D. (2012). Instrumental evidence of normal mode rock slope vibration. *Geophys. J. Int.*, 188:559–569.

Fäh, D., Wathelet, M., Kristekova, M., Havenith, H., Endrun, B., Stamm, G., Poggi, V., Burjanek, J., and Cornou, C. (2009). Using ellipticity information for site characterisation. NERIES deliverable JRA4 D4, available at http://www.neries-eu.org.

Hobiger, M., Bard, P.-Y., Cornou, C., and Le Bihan, N. (2009). Single station determination of Rayleigh wave ellipticity by using the random decrement technique (RayDec). *Geophys. Res. Lett.*, 36.

Joyner, W. B., Warrick, R. E., and Fumal, T. E. (1981). The effect of Quaternary alluvium on strong ground motion in the Coyote Lake, California, earthquake of 1979. *Bull. Seismol. Soc. Am.*, 71(4):1333–1349.

Maranò, S., Reller, C., Loeliger, H.-A., and Fäh, D. (2012). Seismic waves estimation and wavefield decomposition: Application to ambient vibrations. *Geophys. J. Int.*, 191:175–188.

Poggi, V., Edwards, B., and Fäh, D. (2012). Characterizing the Vertical-to-Horizontal ratio of ground motion at soft-sediment sites. *Bull. Seismol. Soc. Am.*, 102(6):2741–2756.

Poggi, V. and Fäh, D. (2010). Estimating Rayleigh wave particle motion from three-component array analysis of ambient vibrations. *Geophys. J. Int.*, 180:251–267.